Published in final edited form as:
Aging Cell. 2013 October ; 12(5): 823–832. doi:10.1111/acel.12112.

Aging results in copper accumulations in GFAP-positive cells in the subventricular zone

Yulia Pushkar[a,1], **Gregory Robison**[a], **Brendan Sullivan**[a], **Wei Zheng**[b], **Sherleen X. Fu**[b], **Meghan Kohne**[a], **Wendy Jiang**[b], **Sven Rohr**[a], **Barry Lai**[c], **Matthew A. Marcus**[d], and **Taisiya Zakharova**[a]

[a]Department of Physics, Purdue University, 525 Northwestern Ave., West Lafayette, IN 47907

[b]School of Health Sciences, Purdue University, 550 Stadium Mall Drive, West Lafayette, IN 47907

[c]X-ray Science Division, Advanced Photon Source, Argonne National Laboratory, Building 401, 9700 S. Cass Ave., Argonne, IL 60439

[d]Advanced Light Source, Lawrence Berkeley National Laboratory, 1 Cyclotron Rd., Berkeley, CA 94720

Abstract

Analysis of rodent brains with X-ray fluorescence (XRF) microscopy combined with immunohistochemistry allowed us to demonstrate that local Cu concentrations are thousands of times higher in the glia of the subventricular zone than in other cells. Using XRF microscopy with subcellular resolution and intracellular X-ray absorption spectroscopy we determined the copper (I) oxidation state and the sulfur ligand environment. Cu K-edge XANES is consistent with Cu being bound as a multimetallic Cu-S cluster similar to one present in Cu-metallothionein. Analysis of age related changes show that Cu content in astrocytes of the SVZ increases 4 fold from 3 weeks to 9 months while Cu concentration in other brain areas remain essentially constant. This increase in Cu correlates with a decrease in adult neurogenesis assessed using the Ki67 marker (both, however, can be age related effects). We demonstrate that the Cu distribution and age-related concentration changes in the brain are highly cell-specific.

Introduction

The brain contains the highest copper (Cu) content in the body next to the liver (1). Serving as a cofactor of key proteins involved in mitochondrial activity, neurotransmitter biosynthesis, oxidative stress defense and other critical brain processes, Cu is essential for normal brain function (2). An abnormal Cu homeostasis, on the other hand, has been implicated in the pathogenesis of various neurodegenerative disorders, including Wilson's disease, Alzheimer's disease, Parkinson's disease, familial amyotrophic lateral sclerosis and prion disorders (3,4). Despite its critical role in brain physiology, knowledge on Cu transport into the brain, its distribution and homeostatic regulation remains limited. There is a consistent body of literature showing increase in brain Cu content with aging (5,6), however, no studies have been conducted with adequate spatial resolution to show whether observed increase is uniform among different brain areas and cells or whether some brain areas/types of cells accumulate Cu to a much greater extent.

[1]To whom correspondence should be addressed: Department of Physics, Purdue University, 525 Northwestern Ave, West Lafayette, IN, USA 47907, Tel: (765)496-3279; Fax: (765) 494-0706; ypushkar@purdue.edu.

It has long been hypothesized that among the parencymal cells astrocytes have greatest influence on Cu homeostasis in the brain (7). It was demonstrated that rat astrocytes in cultures efficiently take up Cu from medium (8,9). Cell culture studies also indicate that neurons are more susceptible to Cu-induced cytotoxicity than astrocytes (10). These studies were done in cell cultures since techniques for tracking Cu ions in particular brain cells were not available.

The Cu content in the brain has frequently been analyzed in relation to neurodegenerative diseases and other pathological conditions (4). The conventional methods for metal quantitation in the brain by atomic absorption spectroscopy, mass spectrometry or utilization of radioactive copper isotopes such as ^{67}Cu, lack spatial resolution. A recent review of neuroimaging techniques, for instance, listed laser ablation inductively coupled plasma mass spectrometry (LA-ICP-MS) as having spatial resolutions ranging between 5-150 μm (11). While such imaging is unquestionably valuable to the medical community, it does not presently achieve resolutions required to explore phenomena on the sub-micron scale for which μXRF is well suited. Secondary ion mass spectrometry (SIMS) has also proven to be a useful tool for biological imaging but has limitations related to a small probe volume. Numerous stains for copper have the required resolution but fail to provide quantitative information. Moreover, neither of the conventional techniques can define the Cu oxidation state. Development of fluorescent sensors to Cu(I) is hindered by the properties of Cu(I) as a strong fluorescent quencher and the low stability of free Cu(I) in water medium. μXRF imaging provides the sensitivity and spatial resolution necessary to reveal the distribution of metals in tissues and single cell.

Application of X-ray fluorescence (XRF) microscopy allowed us to analyze the Cu distribution in rodent brains and to visualize for the first time intracellular Cu accumulations in glial cells as well as follow development of these accumulations with aging. Parallel analysis of neurogenesis show that increase in Cu content in astrocytes in the subventricular zone (SVZ) correlates with decrease in the adult neurogenesis quantified by the Ki67 marker (both, however, can be age related effects). The combination of imaging and X-ray near edge spectroscopy (XANES) techniques allowed us to determine the Cu oxidation state and the ligand environment. From these data it follows that live astrocytes have mechanism to detoxify accumulated Cu, however, if Cu loaded astrocytes would die as a result of brain injury or aging, toxic Cu might be released into environment and affect brain cells.

Materials and Methods

Animals

Male Sprague–Dawley rats (Harlan, Indianapolis, IN.) were purchased 7-8 weeks old and were housed in a temperature-controlled, 12/12 light/dark room, and allowed free access to pelleted rat chow (Purina rodent chow 5001, 13 ppm Cu content) and distilled, deionized water. Eight week-old mice 129S1/SvImJ were purchased from the Jackson Laboratory. At the age of 12 weeks (rats) and 9 weeks (mice) the animals were sacrificed and the brains were dissected and frozen directly on dry ice. This study used in total 18 animals (6 mice, 12 rats). The rats were purchased at three different occasions with 2 and 3 months intervals between the purchases. Selective Cu enrichment of the SVZ was detected in all animals. For age studies additionally 3 weeks and 9 months old Sprague–Dawley rats (Harlan, Indianapolis) with 3 animals in each age group were used. All experiments complied with animal rights regulations and were approved by the Institutional Committee on Animal Use at Purdue University.

BrdU – injections

5- bromo-2-deoxyuridine (BrdU), the cell proliferation specific marker, can be incorporated into the newly synthesized DNA of replicating cells (during the S phase of cell cycle) in place of thymidine. BrdU was dissolved in saline to final concentration 10 mg per 1 ml. The solution of BrdU was prepared twice in a day and kept on ice. 2 rats 12 weeks old, 350 and 330 g, received 45 mg BrdU daily via five IP injections for 6 consecutive days. Before sacrificing the rats were not injected for 24 hours.

Preparation of brain sections

To prevent sample contamination, all glassware was washed with acid (10% HNO_3) and Teflon-coated microtome blades were used. X-ray compatible substrates were constructed of 4 μm thick polypropylene film stretched on frames or 100 μm thick Si wafers used in cryo-measurements. Coronal sections of 30 μm and 10 μm thickness were cut from frozen brains, thawed on sample supports, frozen immediately, and stored at −80°C until analysis. Coronal sections with lateral ventricles were identified by staining with cresyl violet and collected. No chemical fixation was used. Samples were XRF imaged at room temperature and at 80 K showing the same pattern of Cu distribution. To minimize X-ray induced damage to the brain samples, each pixel was measured for less than 1 s (Table 1). Cresyl violet staining of samples after room temperature XRF microscopy showed an overall preserved sample structure (Fig. 1E).

Synchrotron based XRF

The parameters of the XRF experiments are summarized in Table 1. A description of the Advanced Light Source Beamline 10.3.2, can be found in (12). Cu K_α fluorescence counts were recorded by a 7-element UltraLEGe detector and compared to a thin Cu film standard. A description of the 2-ID-D beamline of the Advanced Photon Source can be found in (13) and the BioCAT beamline in (14). Using the program MAPS (15), the spectrum at each pixel was individually fitted to remove overlaps between adjacent K_α / K_β emission lines. Conversion of elemental fluorescence intensities to areal densities in $\mu g/cm^2$ was performed by comparing the XRF intensities with those from thin film standards NBS-1832 and NBS-1833 (NIST, Gaithersburg, MD). The results of the Cu quantitation are summarized in Table 2. To analyze the Cu concentration in the intracellular compartments, areas containing Cu “hot spots” were selected by identifying the pixel with maximal Cu content and then taking into consideration all pixels with a Cu content higher or equal to half the maximum. The average Cu concentrations were then obtained using these selected pixels.

To compare the Cu content in the SVZ of rodents of different age we employed median thresholding to isolate Cu hot spots occurring in astrocytes. Median thresholding compares the observed concentration to the local baseline concentration by taking the difference between that pixel’s concentration and the median of a 30 × 30 μm^2 box around that pixel, resulting in a peak concentration map. Analysis of hot spots was carried out using pixels within 90% of the maximum intensity.

Cryogenic XRF and XANES

A Linkam cryostage with a programmable temperature controller unit was mounted on the motorized stage at ALS beamline 10.3.2 and set to 80 K. Brain samples on 100 μm thick Si wafers, designed for optimal thermal conductivity and tight contact with the silver cold block of the cryostage, were placed on the cryostage via the sample port to prevent thawing. For energy calibration of the Cu K-edge XANES, Cu foil was used with E_0=8980.48 eV, while internal scan-to-scan calibration was done using a monochromator glitch.

Immunohistochemical staining

Frozen (−80 °C) brain sections on microscope slides or on 4 μm polypropylene film were thawed, fixed with 4% paraformaldehyde (PFA) in phosphate buffered saline (PBS) for 5 (MT), 15 (Ki67), or 30 (GFAP) minutes at room temperature (RT), washed twice with PBS, treated for 1 hour at RT sequentially with: 1) blocking/ permeabilization solution: (2% (w/v) bovine serum albumin (BSA) / 0.2% (v/v) Triton X-100 in PBS), 2) primary antibodies in PBS containing 2% BSA at dilutions specified in the reagents listing, 3) secondary antibodies in PBS containing 2% BSA: either Alexa Fluor 488 goat anti-rabbit IgG at 1:1000 dilution for optical microscopy or Nanogoldgold 1.4nm anti-rabbit IgG Au nanoparticles 1:120 dilution for XRF microscopy. Three, five minute washes with PBS were performed after treatment with primary and secondary antibodies. Sections on microscope slides were subjected to ProLong Gold antifade reagent before being covered with a coverslip. Slides were sealed and stored at 4 °C. To visualize immunochemical staining a Nikon Eclipse TE2000-U fluorescence inverted microscope was used. Sections on 4 μm polypropylene film were XRF imaged immediately after staining and optical imaging. Treatments of brain tissue during staining result in partial Cu loss and increased Cu background in the tissue as compared to fresh, untreated sections.

Reagents: anti-GFAP rabbit polyclonal (Invitrogen 18-0063, 1:200); anti-Ki67 rabbit polyclonal (abcam ab15580, 1:300); Anti-metallothionein mouse monoclonal (abcam ab12228, 1:150); Alexa Fluor 488 goat anti-mouse IgG (Invitrogen A-11029); Alexa Fluor 488 goat anti-rabbit IgG, highly cross-adsorbed (Invitrogen, A-11034); Anti-rabbit IgG 1.4 nm Au nanoparticle conjugates (Nanoprobes #2003); BSA (Sigma, A4503); Triton X-100 (Sigma, T9284); ProLong Gold antifade reagent (Invitrogen, P36930).

Preparation of 6Cu(I)-Metallothionein I/II sample for XANES (16)

All steps for preparing 6Cu(I)-Metallothionein (MT) complex were performed in a glove box at anaerobic conditions. Apo-Metallothionein (1A/2B mixture) was purchased from Bestenbalt LLC (#031-2000) and dissolved to 1.6 mM in Tris-HCl buffer, pH 7.8. To reduce oxidized apo-MT, dithiothreitol (DTT) was added at a concentration of 48 mM (ratio DTT:MT = 30) and the mixture was incubated for 1 hour at RT. To remove excess DTT, 100 μL of apo-MT and DTT mixture was loaded into a small G-25 sephadex column, equilibrated with 0.01 HCl, and 1.3 ml of reduced apo-MT was collected (final concentration ~ 0.12 mM). Cu(I)Cl at 10 mM was prepared in a solution of 0.1N HCl and 4% NaCl and added to reduced apo-MT at ratio 6:1. The mixture was incubated for 30 minutes at RT. After incubation, pH was adjusted with Tris/HCl to pH 7.8. Cu(I)-bound MT was concentrated using an Amicon Ultra-4, PLBC Ultracel-3 Membrane, 3 kDa centrifugal filter unit (Millipore, UFC800324) up to ~ 3 mM. Holders for XAS were filled with the concentrated sample and placed immediately in a −80C freezer.

Quantification of neurogenesis by Ki67

Fluorescing cells were counted as follows: pixels with a fluorescence intensity above a pre-determined threshold (as shown in Fig. 4) which were isolated were considered to be a single cell. To normalize for variations in the ventricle size due to age, the number of fluorescing cells was divided by the length of the ventricle, resulting in cell/μm units to express number of actively dividing cells. The ventricle length was determined from the differential image contrast (DIC) micrograph with lengths derived from a camera calibration slide. The ventricle's lack of tissue provided sufficient contrast to readily determine the length using the DIC micrograph. Analysis was carried out on three animals at each age (3, 12, 16, and 36 weeks).

Results

Visualization of Cu distribution in rat and mice brains by X-ray Fluorescence Imaging

The Cu distribution in coronal sections of rodent brains is displayed in Fig. 1. Numerous steps were taken to prepare the brain samples without introducing artifacts that may affect the Cu distribution and speciation (Materials and Methods). In Fig. 1, the Cu K_α (Fig. 1B-D) fluorescence maps are displayed for each pixel. In rat brain, Cu accumulations were detected along the ventricle walls, in the external capsula, and in the septofimbrial and triangular nuclei. In particular, a considerably elevated Cu content was noted along the lateral ventricle wall (17,18). Imaging of the lateral ventricle with increased spatial resolution (Fig. 1D) allowed for visualization of the choroid plexus and demonstrated that the Cu enrichment is localized in the subventricular zone (SVZ). Local variations in Cu fluorescence suggested intracellular Cu accumulation.

X-ray Fluorescence Microscopy and Identification of the Cell Types

XRF microscopy with subcellular resolution on rodent brains revealed Cu accumulations in cells of the SVZ. For analysis of the intracellular Cu distribution we sampled cells in the second to fourth cell layers from the ventricle wall of 10 μm thick coronal sections (Fig. 2, S2). XRF microscopy provided markers of the cell structures. For instance, cell nuclei were identified by increased phosphorous signals, while sulfur and iron were distributed throughout the cytoplasm. Potassium was concentrated inside the cell, thus helping to define the overall cell shape. XRF microscopy clearly showed Cu rich accumulations up to 1 micron in size and with Cu concentrations on the order of hundreds of mM (Tables 2, 3). Cu accumulations were detected in close proximity to cell nucleus (visualized by increased phosphorus signal) as well as at considerable (up to 5μm) distance from nucleus. Remarkably, the detected Cu rich accumulations had low concentration of other metals such as Zn and Fe (Fig. 2A, S2). Lack of co-localization with Zn eliminates the possibility that they originate from Cu/Zn superoxide dismutase 1 enzyme. Co-localization of the Cu signal with S was prominent in all positions of increased Cu content (Fig. 2A, S2). Linear fits of correlation curves (Fig. 2B) allowed us to estimate the S/Cu molar ratios in the range of 1.1 to 1.5 (Table 3). This ratio could be underestimated, as low-energy S fluorescence can be more readily reabsorbed by the sample; 10 μm of H_2O (to model tissue) absorbs 35% of S K_α and 1% of Cu K_α photons. Low S/Cu molar ratios are possible for Cu ions bound to relatively low molecular weight proteins such as metallothionein and Cox17 or to polypeptide glutathione (note that large molecular weight proteins will have additional Cys and Met amino acids contributing to total S content). In these molecules Cu is bound in the form of multimetallic clusters where sulfur atoms bridge between Cu ions, resulting in low S/Cu ratios.

XRF-microscopy with subcellular resolution demonstrated that not all cells in the SVZ contained the Cu enriched accumulations (Fig. 1-2). This is due to the heterogeneous cellular composition of the SVZ with four types of cells: ependymal, GFAP-expressing astrocytes - type B progenitors, type C transit amplifying cells and type A migrating neuroblasts, comprising about 95% of its cell population (19-21). Co-localization of Cu XRF with optical and XRF-IHC fluorescence of immunochemically stained glial fibrillary acidic protein (GFAP), a marker of GFAP expressing astrocytes, demonstrated that Cu is preferentially localized in the GFAP positive cells (Fig. 1F, 3A,B, S1). For Cu occurring in cell bodies we observed prominent GFAP/Cu co-localization due to bright GFAP stain of the cell bodies. Weaker GFAP stain of processes also shows co-localization with Cu when GFAP is visualized at decreased dark level. These results are in agreement with Cu / P distributions showing Cu accumulations at significant distances from cell nucleus (Fig. S1, S2).

Injection of rats with the proliferation marker bromodeoxyuridine (BrdU) (see Materials and Methods) allowed us to identify actively dividing cells of type A and C (Fig. 3C). In the brains of these rats, XRF measurements above the energy of the Br K edge detected the distribution of Br, while measurements in control rats did not detect any Br signal. Selective visualization of nuclei with Br enrichment was done by co-localization of Br and phosphorus signals (Fig. 3C). Moreover, the cells with Br-enriched nucleus were smaller than the others. This is in agreement with earlier studies showing that A-type cells are smaller in size (about 8 μm) than those of the B- or C-type (21). A-type cells are also elongated along the direction of their migration along the ventricle wall (this direction is perpendicular to the plane of the image). While areas occupied by actively dividing cells were mostly free from Cu accumulations, the cells surrounding them showed Cu signals. It is known that type B progenitors surround actively dividing cells of the SVZ (Fig 3C). These data thus support the notion that Cu primarily accumulates in type B progenitors.

Age related changes in Cu content of the SZV astrocytes

Design of a specific experiment to assess the effects of Cu-enrichment in type B progenitors on adult neurogenesis is hindered by the currently unknown mechanisms regulating the Cu deposition in these cells. However, it is well known that adult neurogenesis decreases with age which is manifested in the decrease in the self-renewal capacity and the number of SVZ progenitors (22,23). The mechanisms responsible for the age-related decline in the function of stem cells and other progenitors remain unclear. An analysis of the Cu content in the SVZ of animals from 3 weeks to 9 months old showed a dramatic increase in Cu X-ray fluorescence with increased animal age (Fig. 4). Changes in Cu levels with age were analyzed by measuring two different characteristics: averaged Cu concentration in SVZ (defined as 100 μm layer along the ventricle wall), (Fig. 4B) and Cu concentration in the hot spots (determined by median thresholding, see Material and Methods), Fig. 4C. Observed increase in Cu concentrations with age was fitted to two models: linear dependence and monomolecular growth. For increase of averaged Cu concentration (Fig. 4B) in SVZ the data were best described ($R^2 = 0.944$) by monomolecular growth: [Cu] = 80.08(1-exp(−(a + 1.377 wk)/18.03wk) (mM) while increase in Cu concentration in the hot spots was best described by linear fit. Critical increases in Cu content of the SVZ were compared with data for cortex (Fig 4B), where essentially no large changes in Cu content were detected. Considering the mean Cu concentration over an entire 30μm thick coronal half-section also showed a very small increase of Cu concentration with respect to age as compared with growth in the SVZ.

Increased Cu concentration was correlated with a decrease in adult neurogenesis (Fig. 4D) quantified by IHC for Ki67 proliferation marker (see Material and Methods). Strong linear correlations were obtained for both cases of measuring averaged Cu concentration r=-0.89 correlation (Pearson) as well as measuring increase in intensity of Cu hot spots r=-0.99 (Fig. 4D).

Identification of the Cu oxidation state and coordination environment by Micro-X-ray Absorption Near Edge Spectroscopy (XANES)

Information on the copper's oxidation state and ligand environment is critical to elucidate the mode of its intracellular binding and its biological role in the cell. Cu(I) K-edge XANES is known to exhibit an intense feature at ~8983 eV corresponding to an electric dipole-allowed 1s-to-4p transition. The intensity of this transition is sensitive to the occupancy of the Cu 4p orbitals which differs according to the coordination (i.e. diagonal, trigonal, tetragonal, etc.). The shape and intensity of this feature can be used to determine the coordination environment of the Cu(I) site in proteins (24,25). XANES on the intracellular Cu rich accumulations was recorded at low (80 K) temperature ensuring non-damaging

conditions (Fig. 5). Spectra obtained from different Cu enriched accumulations were the same within signal-to-noise. This demonstrated that Cu inside different accumulations has the same binding environment. The energy of the Cu K-edge unambiguously identified the Cu oxidation state as Cu(I). A comparison of the obtained XANES spectrum with spectra of model Cu compounds and Cu bound proteins available in the literature showed that it was characteristic for the Cu (I)-thiolate multimetallic cluster and closely resembled the spectra published for a variety of Cu-MTs (25). The work of Pickering *et. al.* (25) illustrates that details of Cu XANES spectra are different for different proteins containing Cu (I)-thiolate multimetallic clusters. This is not surprising as the electronic structure of the metal clusters in proteins is known to be affected by the protein environment. In Cu XANES the number of transitions and their relative intensities are sensitive to the electronic structure of the Cu_xS_y cluster. Assignment to Cu (I)-thiolate multimetallic cluster agrees with the identification of a predominantly sulfur coordination environment from co-localization of the Cu and S signals from XRF microscopy. Comparison of the Cu XANES spectra from the intracellular compartments with the spectrum of Cu-MT prepared from rabbit apo-metallothionein (Materials and Methods) and recorded at the same experimental conditions demonstrated a high degree of similarity (Fig. 5).

Discussion

Serving as a cofactor of key proteins involved in mitochondrial activity, neurotransmitter biosynthesis, oxidative stress defense and other critical brain processes, Cu is essential for brain development and metabolism as well as for learning and memory (2). Recently Cu distribution in the rodent brains were analyzed with intermediate spatial resolution (150-40 μm) and increase in Cu concentration in subventricular areas were noted (17,18). However, no elaboration was presented on cellular origins of detected Cu. Here we present the first quantitative imaging analysis of the Cu distribution in rodent brains with subcellular resolution combined with IHC. The outcome of the XRF microscopy analysis is the detection of significant local accumulations of this potentially toxic metal ion in astrocytes. These accumulations are detected in healthy animals in normal physiological conditions suggesting that astrocytes have a capacity for safe handling of high Cu content. These results reinforce earlier hypothesis of Cu localization to glia cells based on histochemical and kinetic studies on Cu distribution in the brain (26). Dynamic studies of Cu release are very intriguing and imply a capability for cell-cell Cu transfer with possible participation of astrocytes (27,28). Here, XRF techniques allowed for exact quantitative imaging of Cu inside the astrocytes.

Despite its critical role, knowledge of Cu transport into the brain, its distribution and homeostatic regulation remains limited. Like any mammalian cells, astrocytes uptake Cu into the cytoplasm by the copper transporter 1 (Ctr1). Ctr1 passes Cu to Cu chaperones, which mediate the intracellular transport of Cu to Cu proteins via mechanisms utilizing direct protein-protein interaction. Possible pathways for the Cu transport into the astrocytes include Cu absorption either from the blood or the cerebrospinal fluid (CSF). Astrocytes have perivascular endfeet or foot-plates, expanses of their cytoplasmic processes that surround the abluminal surfaces of the capillary endothelial cells that form the blood brain barrier (BBB) of the brain and are opposed to the endothelial basal lamina (29). The BBB is partially lost on the surface of blood capillaries in the SVZ (30) which can explain highest Cu accumulations detected in astrocytes positioned close to the ventricle wall. The choroid plexus, a tissue in brain ventricles adjunct to the SVZ, transports Cu and other metals between the blood and the CSF (31). The CSF is separated from the cells of the SVZ by only one layer of ependymal cells, which, to the best of our knowledge, do not form tight junctions. Some of the type B progenitors retain direct exposure to the surface of the ventricle wall even in adults (32). Thus, astrocytes have preferential (as compared to

neurons) access to the interstitial fluids as well as the CSF. Observation of the extensive Cu accumulations in the astrocytes of the SVZ and partially in the ependymal cells might lead to the idea that cells in this part of the brain function as an additional barrier between systemic fluids and brain tissues (at least in terms of Cu transport). In such a case, accumulation of Cu can be envisioned as a result of Cu retention at this barrier. However, we think that this is an unlikely function and that the astrocytes are rather balancing the Cu content in the brain to meet the brain's Cu needs than simply achieving Cu detoxification. In support of such a view speaks our observation that the local Cu concentration in the astrocytes is several orders of magnitude higher than those in the blood and CSF (Table 2) which would imply a facilitated Cu uptake and retention. Moreover, the concentrations of other possibly toxic metals such as Zn, Mn and Fe are not increased in these cells as compared with brain cells at other locations (Fig. 2), showing that other metal ions are not accumulated at this potential barrier. This therefore implies that astrocytes are uniquely capable of absorbing and retaining Cu ions. The ability of astrocytes to retain Cu might also relate to the fact that these cells do not express the ATP7B Cu transporter responsible for Cu export from the cell (33).

The essentially linear increase of Cu concentration in hotspots with age as compared to baseline Cu levels suggests that the mechanism responsible for accumulating Cu is unyielding with time, at least through the ages probed in this study. It has been argued that since natural selection governs metal homeostasis only through reproductive and care-giving ages, neurological mechanisms are not well optimized for aged life; the manifestation of the resulting unoptimized metal concentrations is neurodegenerative disease (34). Previous studies have established that Cu homeostasis in rats is requisite for reproduction (35) and that trace levels of Cu are necessary to perform functions required for healthy brain development (2). We observe that migrating neuroblasts lack Cu accumulations implying these have been dissolved/consumed during cell division. Thus, the machinery regulating Cu homeostasis, including Cu stores in the SVZ, in young rodents must be robust to allow sufficient Cu for cell divisions. If that depositing mechanism is never turned off after reproductive ages, however, Cu stores in astrocytes may grow unwieldy. Elevated oxidative stress caused by increased content of redox active metal ions, which has been implicated in Alzheimer's disease, Parkinson's disease, and several other neurodegenerative disorders (3), may be capable of preventing proliferation, explaining the observed correlation between peak Cu concentrations and neurogenic rates (Fig. 4D).

Taking into account how dangerous elevated Cu levels can be better understanding of Cu-binding/sequestration in astrocytes is critical. Intracellular Cu K-edge XANES measurements are instrumental in this regard. The high degree of similarity between the XANES spectra of intracellular Cu in astrocytes and those of prepared Cu-MT suggests that Cu is bound to MT or protein providing similar Cu binding environment with the formation of multimetallic Cu-S cluster. One of the hallmarks of a multimetallic Cu(I)-S cluster XANES spectrum a monotonic increase of absorbance with energy near the Cu K edge (8046 eV) due to the Cu-Cu binding. There are numerous examples in the literature (e.g., (36,37)) which compare Cu-S clusters to model compounds with only one Cu that exhibit decreased absorbance immediately following the edge. Since both of our spectra exhibit increasing absorbance at the edge, it is concluded that the Cu is bound in the form of multimetallic cluster. Results of Table 3 illustrate that [S]/[Cu] ratio is comparable to the one expected for Cu-MT. High local Cu concentrations (100-500 mM, Table 2) can indicate potential aggregates and MT has been shown to form aggregates with Cu in pathological conditions (38). In the brain, astrocytes are the main source of MT I, and II, although other cell types, such as choroid plexus epithelium, endothelium and meningeal cells, may also show MT I and II expression (39,40). Astrocytes of the SVZ show intense MT I, II expression detected by in situ hybridization and immunohistochemistry (41,42), (Fig. 1G)

Metallothionein, a ubiquitously occurring low molecular weight cysteine-rich protein, is involved in numerous physiological processes including metal ion homeostasis, oxidative stress defense and stimulation of neurite growth (43). The role of the Cu-MT complex in detoxification of intracellular copper is well established. For instance, pathological hallmarks of copper overload are Cu-metallothionein depositions in the lysosomes of hepatocytes in Wilson's disease patients and animal models of Cu-overload (38,44). One of the therapies received by Wilson's disease patients, whose organisms cannot effectively excrete Cu due to a genetic defect in the ATP7B Cu-transporter, induces metallothionein to facilitate Cu-binding. While we have not confirmed that Cu accumulations are bound to MT, such an assignment is consistent with current literature. Assignment of the protein nature will be confirmed in the future by analysis of MT(I,II) knock out animal.

Our data give a quantitative analysis of the Cu distribution and speciation in the brain and highlight the existence of an efficient Cu-accumulation mechanism in the astrocytes. This mechanism should allow astrocytes to play the role of "Cu-buffering" cells in the brain. Astrocytes are likely maintaining Cu homeostasis in the brain and disruption of their functions might result in the release of toxic Cu. It is currently not known how the Cu handling by the astrocytes is changing under various pathological conditions. Quantitative imaging techniques with sub-cellular resolution will thus be a key in studies of the role of copper in brain development and normal functionality as well as in various pathological conditions such as stroke, brain tumors, neurodegenerative diseases, and genetic diseases of Cu metabolism (Menkes and Wilson's diseases). μXRF microscopy is a powerful technique for such analysis.

Supplementary Material

Refer to Web version on PubMed Central for supplementary material.

Acknowledgments

We greatly acknowledge the Bio-CAT beamline at APS for providing the Linkam cryostage and Dr. Raul Barrea and Dr. Stefan Vogt for helpful discussions. The operations of the ALS at LBNL are supported by the Director, Office of Science, Office of Basic Energy Sciences, U.S. Department of Energy under contract number DE-AC02-05CH11231. Use of the APS at ANL was supported by the U. S. Department of Energy, Office of Science, Office of Basic Energy Sciences, under Contract No. DE-AC02-06CH11357. The Biophysics Collaborative Access Team is a National Institutes of Health (NIH) supported Research Center RR-08630.This study was supported by NIH/National Institute of Environmental Health Sciences Grants Numbers R01 ES008146-14, by Purdue start up funds and by NSF summer research experience for undergraduates program to M.K.

References

1. Bush AI. Metals and neuroscience. Curr. Opin. Chem. Biol. 2000; 4:184–191. [PubMed: 10742195]
2. Schlief ML, Gitlin JD. Copper Homeostasis in the CNS. Mol. Neurobiol. 2006; 33:81–90. [PubMed: 16603790]
3. Barnham KJ, Bush AI. Metals in Alzheimer's and Parkinson's diseases. Curr. Opin. Chem. Biol. 2008; 12:222–228. [PubMed: 18342639]
4. Astrid Sigel, HS.; Sigel, Roland K. O., editors. Neurodegenerative Diseases and Metal Ions. Wiley; 2006.
5. Palm R, Wahlström G, Hallmans G. Age related changes in weight and the concentrations of zinc and copper in the brain of the adult rat. Lab. Anim. 1990; 24:240–245. [PubMed: 2395323]
6. Massie HR, Aiello VR, Iodice AA. Changes with age in copper and superoxide dismutase levels in brains of C57BL/6J mice. Mech. Ageing Dev. 1979; 10:93–99. [PubMed: 449425]
7. Tiffany-Castiglioni E, Hong S, Qian Y. Copper handling by astrocytes: Insights into neurodegenerative diseases. International Journal of Developmental Neuroscience. 2011; 29:811–818. [PubMed: 21968186]

8. Qian YC, Tiffanycastiglioni E, Harris ED. Copper Transport and Kinetics in Cultured C6 Rat Glioma-Cells. Am. J. Physiol.-Cell Physiol. 1995; 269:C892–C898.
9. Scheiber IF, Mercer JFB, Dringen R. Copper accumulation by cultured astrocytes. Neurochem. Int. 2010; 56:451–460. [PubMed: 20004225]
10. Reddy PVB, Rao KVR, Norenberg MD. The mitochondrial permeability transition, and oxidative and nitrosative stress in the mechanism of copper toxicity in cultured neurons and astrocytes. Lab. Invest. 2008; 88:816–830. [PubMed: 18591939]
11. Bourassa MW, Miller LM. Metal imaging in neurodegenerative diseases. Metallomics. 2012; 4:721–738. [PubMed: 22797194]
12. Marcus MA, MacDowell AA, Celestre R, Manceau A, Miller T, Padmore HA, Sublett RE. Beamline 10.3.2 at ALS: a hard X-ray microprobe for environmental and materials sciences. J. Synchrot. Radiat. 2004; 11:239–247.
13. Cai Z, Lai B, Yun W, McNulty I, Khounsary A, Maser J, Ilinski P, Legnini D, Trakhtenberg E, Xu S, Tieman B, Wiemerslage G, Gluskin E. Performance of a high-resolution x-ray microprobe at the advanced photon source. Synchrotron Radiation Instrumentation. 2000; 521:31–34.
14. Barrea, R.; Gore, D.; Kondrashkina, E.; Weng, T.; Heurich, R.; Vukonich, M.; Orgel, J.; Davidson, M.; Collingwood, J.; Mikhaylova, A. The BioCAT Microprobe for X-ray Fluorescence Imaging, MicroXAFS and Microdiffraction Studies on Biological Samples. Proc 8th Int Conf X-ray Microscopy IPAP Conf Series; 2006.
15. Vogt S. MAPS: A set of software tools for analysis and visualization of 3D X-ray fluorescence data sets. J. Phys. IV. 2003; 104:635–638.
16. George GN, Winge D, Stout CD, Cramer SP. X-Ray Absorption Studies of the Copper-Beta Domain of Rat-Liver Metallothionein. J. Inorg. Biochem. 1986; 27:213–220. [PubMed: 3760860]
17. Pushkar Y. Synchrotron X-Ray Fluorescent Imaging and Spectroscopy Studies of the Role of Copper in the Stem Cell Niche Architecture of Adult Neural Stem Cells. Biophys. J. 2010; 98:745a–745a.
18. Pushie MJ, Pickering IJ, Martin GR, Tsutsui S, Jirik FR, George GN. Prion protein expression level alters regional copper, iron and zinc content in the mouse brain. Metallomics. 2011; 3:206–214. [PubMed: 21264406]
19. Johansson CB, Momma S, Clarke DL, Risling M, Lendahl U, Frisen J. Identification of a neural stem cell in the adult mammalian central nervous system. Cell. 1999; 96:25–34. [PubMed: 9989494]
20. Doetsch F, Caille I, Lim DA, Garcia-Verdugo JM, Alvarez-Buylla A. Subventricular zone astrocytes are neural stem cells in the adult mammalian brain. Cell. 1999; 97:703–716. [PubMed: 10380923]
21. Doetsch F, GarciaVerdugo JM, AlvarezBuylla A. Cellular composition and three-dimensional organization of the subventricular germinal zone in the adult mammalian brain. J. Neurosci. 1997; 17:5046–5061. [PubMed: 9185542]
22. Molofsky AV, Slutsky SG, Joseph NM, He S, Pardal R, Krishnamurthy J, S. NE, Morrison SJ. Increasing p16INK4a expression decreases forebrain progenitors and neurogenesis during ageing. Nature. 2006; 443:448–452. [PubMed: 16957738]
23. Maslov AY, Barone TA, Plunkett RJ, Pruitt SC. Neural stem cell detection, characterization, and age-related changes in the subventricular zone of mice. J. Neurosci. 2004; 24:1726–1733. [PubMed: 14973255]
24. Kau LS, Spirasolomon DJ, Pennerhahn JE, Hodgson KO, Solomon EI. X-Ray Absorption-Edge Determination of the Oxidation-State and Coordination-Number of Copper - Application to the Type-3 Site in Rhus-Vernicifera Laccase and Its Reaction with Oxygen. J. Am. Chem. Soc. 1987; 109:6433–6442.
25. Pickering IJ, George GN, Dameron CT, Kurz B, Winge DR, Dance IG. X-Ray-Absorption Spectroscopy of Cuprous Thiolate Clusters in Proteins and Model Systems. J. Am. Chem. Soc. 1993; 115:9498–9505.
26. Szerdahelyi P, Kasa P. Histochemical-Demonstration of Copper in Normal Rat-Brain and Spinal-Cord - Evidence of Localization in Glial-Cells. Histochemistry. 1986; 85:341–347. [PubMed: 2428777]

27. Hartter DE, Barnea A. Brain-Tissue Accumulates Copper-67 by 2 Ligand-Dependent Saturable Processes - a High-Affinity, Low Capacity and a Low Affinity, High-Capacity Process. J. Biol. Chem. 1988; 263:799–805. [PubMed: 3335527]
28. Dodani SC, Domaille DW, Nam CI, Miller EW, Finney LA, Vogt S, Chang CJ. Calcium-dependent copper redistributions in neuronal cells revealed by a fluorescent copper sensor and X-ray fluorescence microscopy. Proc. Natl. Acad. Sci. U. S. A. 2011; 108:5980–5985. [PubMed: 21444780]
29. Abbott NJ, Ronnback L, Hansson E. Astrocyte-endothelial interactions at the blood-brain barrier. Nat. Rev. Neurosci. 2006; 7:41–53. [PubMed: 16371949]
30. Tavazoie M, Van der Veken L, Silva-Vargas V, Louissaint M, Colonna L, Zaidi B, Garcia-Verdugo JM, Doetsch F. A Specialized Vascular Niche for Adult Neural Stem Cells. Cell Stem Cell. 2008; 3:279–288. [PubMed: 18786415]
31. Zheng W, Aschner M, Ghersi-Egea JF. Brain barrier systems: a new frontier in metal neurotoxicological research. Toxicol. Appl. Pharmacol. 2003; 192:1–11. [PubMed: 14554098]
32. Mirzadeh Z, Merkle FT, Soriano-Navarro M, Garcia-Verdugo JM, Alvarez-Buylla A. Neural stem cells confer unique pinwheel architecture to the ventricular surface in neurogenic regions of the adult brain. Cell Stem Cell. 2008; 3:265–278. [PubMed: 18786414]
33. Barnes N, Tsivkovskii R, Tsivkovskaia N, Lutsenko S. The copper-transporting ATPases, Menkes and Wilson disease proteins, have distinct roles in adult and developing cerebellum. J. Biol. Chem. 2005; 280:9640–9645. [PubMed: 15634671]
34. Brewer GJ. Iron and copper toxicity in diseases of aging, particularly atherosclerosis and Alzheimer's disease. Exp. Biol. Med. 2007; 232:323–335.
35. Bedwal RS, Bahuguna A. Zinc, copper and selenium in reproduction. CMLS. 1994; 50:626–640.
36. George GN, Byrd J, Winge DR. X-ray absorption studies of yeast copper metallothionein. J. Biol. Chem. 1988; 263:8199–8203. [PubMed: 3286647]
37. Bogumil R, Faller P, Binz P-A, Vašák M, Charnock JM, Garner CD. Structural characterization of Cu(I) and Zn(II) sites in neuronal-growth-inhibitory factor by extended X-ray absorption fine structure (EXAFS). European Journal of Biochemistry. 1998; 255:172–177. [PubMed: 9692916]
38. Lerch K, Johnson GF, Grushoff PS, Sternlieb I. Canine Hepatic Lysosomal Copper Protein - Identification as Metallothionein. Arch. Biochem. Biophys. 1985; 243:108–114. [PubMed: 4062298]
39. Fuller CE, Elmes ME, Jasani B. Age-Related-Changes in Metallothionein, Copper, Copper-Associated Protein, and Lipofuscin in Human Liver - a Histochemical and Immunohistochemical Study. J. Pathol. 1990; 161:167–172. [PubMed: 2380808]
40. Michalska AE, Choo KHA. Targeting and Germ-Line Transmission of a Null Mutation at the Metallothionein I-Loci and Ii-Loci in Mouse. Proc. Natl. Acad. Sci. U. S. A. 1993; 90:8088–8092. [PubMed: 8367468]
41. Choudhuri S, Kramer KK, Berman NEJ, Dalton TP, Andrews GK, Klaassen CD. Constitutive Expression of Metallothionein Genes in Mouse-Brain. Toxicol. Appl. Pharmacol. 1995; 131:144–154. [PubMed: 7878670]
42. Nishimura N, Nishimura H, Ghaffar A, Tohyama C. Localization of Metallothionein in the Brain of Rat and Mouse. J. Histochem. Cytochem. 1992; 40:309–315. [PubMed: 1552172]
43. Penkowa M. Metallothioneins are multipurpose neuroprotectants during brain pathology. Febs J. 2006; 273:1857–1870. [PubMed: 16640552]
44. Nartey N, Frei J, Cherian M. Hepatic copper and metallothionein distribution in Wilson's disease (hepatolenticular degeneration). Laboratory investigation; a journal of technical methods and pathology. 1987; 57:397.
45. Zheng W, Jiang YM, Zhang YS, Jiang WD, Wang XQ, Cowan DM. Chelation therapy of manganese intoxication with para-aminosalicylic acid (PAS) in Sprague-Dawley rats. Neurotoxicology. 2009; 30:240–248. [PubMed: 19150464]

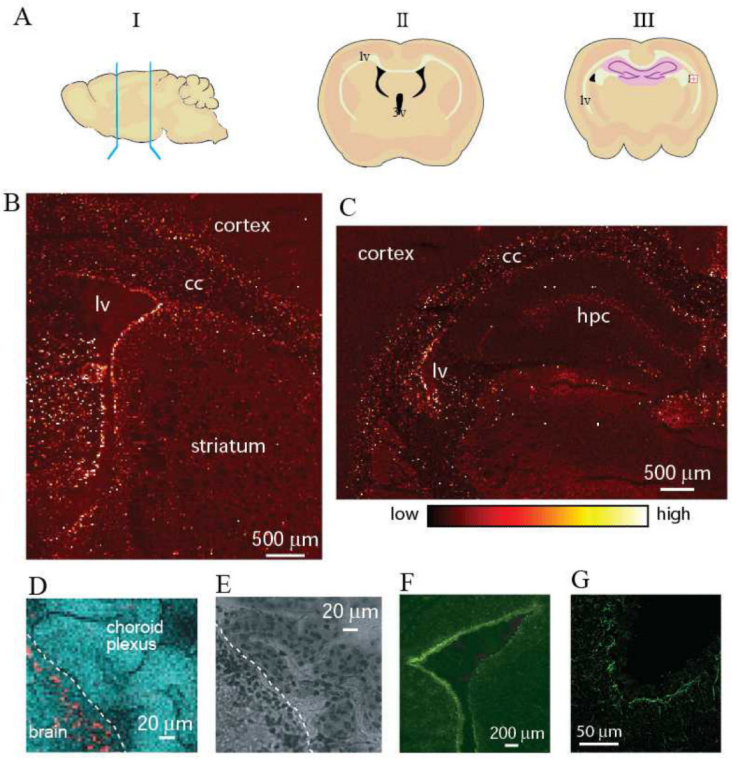

Figure 1.

A. Schematic sagittal and coronal views of a rodent brain showing the area of the brain where sections were collected. The lateral (lv) and third (3v) ventricles are depicted in black. The ventricles contain cerebrospinal fluid (CSF) and cells of the choroid plexus comprising the blood-CSF barrier. **B.** Cu K_α fluorescence map of a rat coronal section at bregma = −0.8. **C.** Cu K α fluorescence map of a rat coronal section at bregma = −2.56. **D.** Coronal section of a rat brain recorded with increased resolution along the ventricle wall showing that the Cu signal in the SVZ has a highly uneven intensity suggesting subcellular Cu localization. Cu K_α fluorescence is shown in red while Compton scattering is in cyan. The white dashed line indicates the ventricle wall. Experimental details are shown in Table 1. Similar distributions were observed in all wild type animals used in this study (6 mice and 10 rats). **E.** Image of the same section as in Fig. 1D after XRF analysis at room temperature stained with cresyl violet demonstrates tissue integrity after exposure to X-rays. **F.** Fluorescence microscopy image of the adjunct coronal section treated with the antibody to glial fibrillary acidic protein (GFAP), a marker of astrocytes. **G.** Fluorescence microscopy image of the SVZ treated with the antibody to Metallothionein I,II (MT).

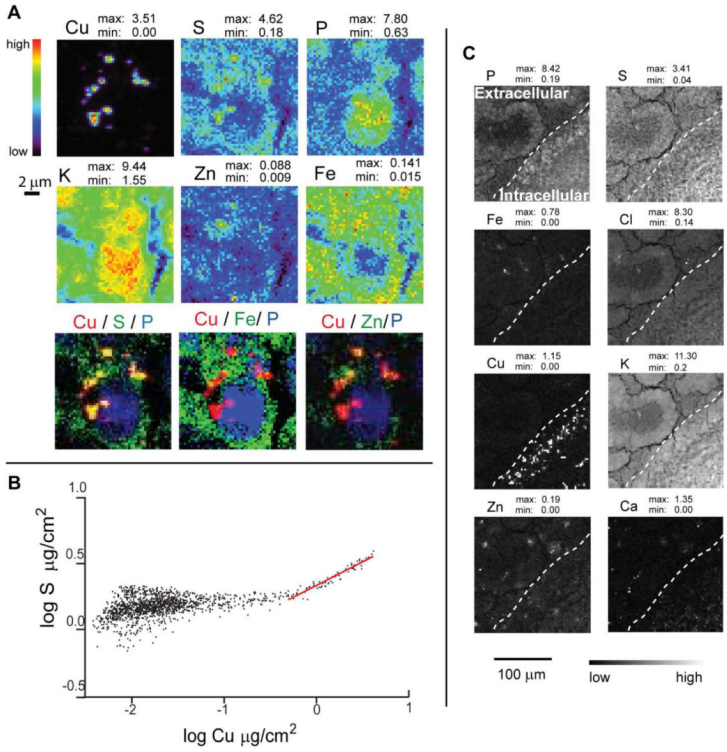

Figure 2.

A. XRF image of the SVZ. Elemental concentrations are in µg / cm^2 in 10 µm thick sections; experimental details are given in Table 1. The dashed line shows the ventricle wall with brain tissue in the right low corner. From XRF imaging it is evident that SVZ selectively accumulates Cu over other trace elements. **B.** A linear fit of the Cu/S correlation allows estimation of the S/Cu molar ratio (Table 3) suggesting that the coordination of Cu is accomplished by sulfur ligands. **C.** XRF microscopy clearly demonstrates intracellular structures with dramatically increased Cu content. The cell nucleus is identified by the increased phosphorous signal, while sulfur is distributed throughout the cytoplasm. Potassium has much higher concentration inside the cell than outside and, thus, helps to define the overall cell shape. The three-color plots in Fig. A show that Cu co-localizes with S. Elemental contents are given in µg/cm^2.

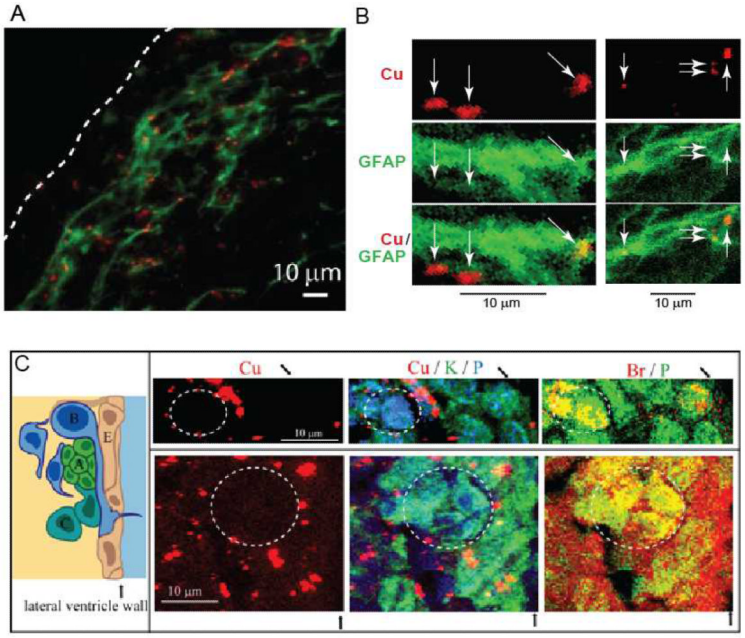

Figure 3.

A. Co-localization of optical fluorescence of immunochemically stained GFAP (green) and X-ray fluorescence from Cu (red). The white dashed line indicates the ventricle wall. **B.** Subcellular colocalization of Cu with GFAP as visualized by immunostaining with gold nanoparticles as a secondary antibody. **C.** Left: Schematic of the cellular architecture of the SVZ. Progenitor cells (A-C) in the SVZ lie adjacent to the ependymal cell (E) layer lining the lateral ventricles. Right: µXRF image of cells located in the SVZ of a Sprague–Dawley rat treated with BrdU – a marker of actively dividing cells. BrdU identifies type A cells - migrating neuroblasts and type C cells - transit amplifying cells. Co-localization of Br and phosphorus X-ray fluorescence signals shows actively dividing cells (dashed circles). Areas occupied by dividing cells have a diminished number of Cu-accumulations. The black arrows indicate the ventricle wall.

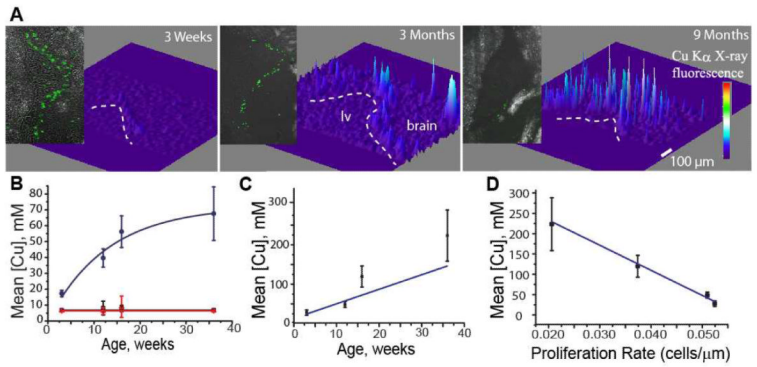

Figure 4.

A. 3D visualization of normalized Cu K_a fluorescence demonstrates an increased copper signal along the lateral ventricle (lv) wall (indicated by the white line) with increased age. Data were obtained from 30 mm thick coronal sections of the brains of 3 weeks, 3 months and 9 months-old rats. Similar distributions were observed in all 9 animals (3 in each age group) used in this study. Experimental details are shown in Table 1. Insets show visualization of Ki67 proliferation marker. **B.** Circles (blue): Mean Cu concentration in the SVZ as a function of age. Solid line shows fit to monomolecular growth model ($R^2 = 0.944$). Squares (black): Mean Cu concentrations in the cortex of the brain. Triangles (red): Mean Cu concentrations of a half-brain coronal section. The solid line in the latter two cases shows a linear regression. It is apparent from this plot that Cu accumulation in the brain happens largely in the SVZ throughout aging. **C.** Cu concentrations in the SVZ Cu hotspots determined by median thresholding. The linearity may suggest that Cu accumulation above baseline levels is carried out by a mechanism which does not change its deposition rate with time ($R^2 = 0.56$). **D.** Correlation between the Cu concentrations in the SVZ Cu hotspots and proliferation rate ($r = -0.99$).

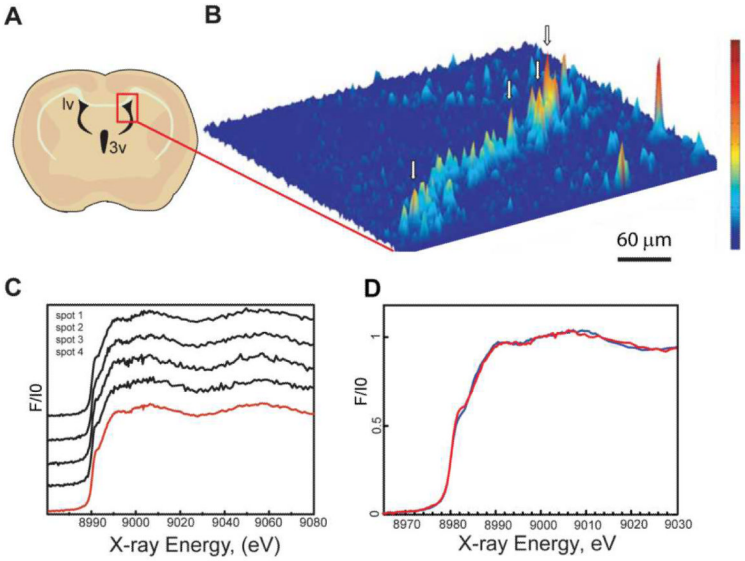

Figure 5.

A. Schematic diagram of coronal section located at approximately Bregma −0.8. The red box indicates the approximate area of the XRF image. **B.** XRF image of copper distribution demonstrates that Cu enrichment is localized to a thin layer along the lateral ventricle wall. XANES measurements (**C**) were taken on Cu accumulations, indicated by arrows. Experimental details are in Table 1. Spectra obtained from different Cu-accumulations are the same within signal-to-noise. The red line is the average of all XANES measurements taken on this sample. **D.** Intracellular Cu K-edge XANES spectrum at low temperature on the Cu accumulations in a rodent brain (red) recorded at the same experimental conditions as the spectrum of Cu-MT prepared from rabbit apo-MT (blue). The high degree of similarity indicates that Cu is present in brain cells in the form of a Cu (I)-thiolate multimetallic cluster and suggests that MT serves as a Cu binding protein.

Table 1

XRF imaging conditions

Figure	Beamline	Pixel size μm(v)×μm(h)	Beam size μm(v) × μm(h)	Dwell time (sec)	Flux (photons/s)	X-ray energy (keV)
1B, C	APS, 18-ID	20 × 20	5 × 5	0.2	2×10^{13}	10.0
1D	APS, 2-ID-D	3 × 3	0.2 × 0.25	1.0	4×10^{9}	10.0
2A, B, 3A, C, S1, S2	APS, 2-ID-D	0.3 × 0.3	0.2 × 0.25	1.0	4×10^{9}	10.0
3B	APS, 2-ID-D	0.35 × 0.35	0.35 × 0.35	1.0	4×10^{9}	12.0
4A †	ALS, 10.3.2	6 × 6, 3 × 3	6 × 6, 3 × 3	0.5	3.5×10^{8}	11.5
4B, C, D †	APS, 18-ID	5 × 5	5 × 5	0.05	2×10^{13}	10.0

*Tissue sections of 30 μm thickness were analyzed at ALS, 10.3.2 and APS 18-ID-D beamlines, while 10 μm thick sections were used for high resolution measurements at APS, 2-ID-D beamline.

†Sections aged 16 weeks old were imaged at APS 18-ID-D (BioCAT) were used for analysis. All other sections used for analysis in Fig. 4 were imaged at ALS 10.3.2.

Table 2

Quantitation of Cu

Method	Object	Cu concentration
AAS (45)	Plasma	15-20μM
	CSF	0.5μM
μXRF	Localized Cu accumulation in cell	~100-500 mM*
	Area in cell without Cu accumulation	~130-300 μM

*This number is obtained with the assumption that localized Cu accumulation is about 1 μm in diameter and the signal detected in μXRF pixel on 10 μm thick section comes from single accumulation.

Table 3

Results of the linear fits for S / Cu correlation (y = ax + b)

Brain		a ([S]/[Cu] in μg/cm^2)	b	R^2	N	[Cu]* mM	[S]/[Cu] molar ratio
Rat 1	area 1	0.60 ± 0.01	1.40 ± 0.02	0.71	42	237.62 ± 81.8	1.19 ± 0.02
	area 2	0.53 ± 0.01	1.69 ± 0.03	0.65	30	203.00 ± 91.2	1.05 ± 0.02
Rat 2	area 1	0.53 ± 0.00	1.79 ± 0.01	0.71	77	313.16 ± 113.3	1.05 ± 0.00
Rat 3	area 1	0.73 ± 0.01	1.60 ± 0.02	0.86	37	168.38 ± 62.9	1.45 ± 0.02
	area 2	0.52 ± 0.01	1.63 ± 0.02	0.70	36	240.77 ± 95.9	1.03 ± 0.02
	area 3	0.54 ± 0.00	1.62 ± 0.01	0.96	51	341.48 ± 135.3	1.07 ± 0.00
Mouse 1	area 1	0.59 ± 0.00	1.07 ± 0.00	0.95	190	368.24 ± 228.1	1.17 ± 0.00
Mouse 2	area 1	0.54 ± 0.00	1.26 ± 0.01	0.96	120	398.13 ± 173.1	1.07 ± 0.00

N – Number of pixels with high Cu content selected by cluster analysis of XRF images recorded on the brain tissue with single cell resolution.

*Numbers are obtained with the assumption that intracellular compartments are about 1 micron in diameter and the signal detected in XRF pixel on 10 micron thick section comes from single compartment.